A MODEL FOR SEAGRASS SPECIES COMPETITION: DYNAMICS OF THE SYMMETRIC CASE

PABLO MORENO-SPIEGELBERG*⊙ AND DAMIÀ GOMILA⊙

Abstract. We propose a general population dynamics model for two seagrass species growing and interacting in two spatial dimensions. The model includes spatial terms accounting for the clonal growth characteristics of seagrasses, and coupling between species through the net mortality rate. We consider both intraspecies and interspecies facilitative and competitive interactions, allowing density-dependent interaction mechanisms. Here we study the case of very similar species with reciprocal interactions, which allows reducing the number of the model parameters to just four, and whose bifurcation structure can be considered the backbone of the general case. We find that the parameter space can be divided into ten regions with qualitatively different bifurcation diagrams. These regions can be further grouped into just five regimes with different ecological interpretations. Our analysis allows the classification of all possible density distributions and dynamical behaviors of meadows with two coexisting species.

1. INTRODUCTION

Seagrass meadows are key to marine coastal ecosystems [5]. They provide food, protection, and structural support to many marine species [2]. Moreover, seagrass meadows are an important sink of carbon dioxide [8], protect the coastline against strong waves [9, 26], and contribute to nutrient sedimentation. From a socioeconomic point of view, seagrass ecosystems support fishing and human development. During the last decades, a decline in seagrass beds associated with trawling, pollution, global warming, or competition with invasive species, among other anthropogenic effects, has been observed [20, 21, 30]. Preventive, palliative, and restoration measures must be taken to reduce the consequences of this declining [11, 25]. Not only seagrasses are in danger, but about half of the marine ecosystems have also been identified as strongly affected by multiple anthropogenic drivers [12]. No wonder UN has declared with urgency 2021-2030 as the "Decade of Ocean Science for Sustainable Development" as well as the "Decade of Ecosystem Restoration" [25].

Dynamical models provide a framework to study the meadow receding process and to understand the mechanisms that govern the ecosystem dynamics. This can be used to estimate the resilience and alert about the proximity of tipping points, after which vegetation systems collapse. Furthermore, they can also be used to make predictions about the evolution of the meadows under different scenarios. This provides useful information to make decisions in ecosystems management.

Two different approaches have been used to study the dynamics of seagrass meadows. The first is based on microscopic agent based models where information on each plant shoot (and apex) is explicitly computed. The dynamics are defined in these systems as a Markovian process at shoot level, where apices grow and/or branch, generating new shoots and apices, and both die with a given rate [28, 29]. The second approach is based on macroscopic models where only spatial densities are considered [23, 24]. In these models, the evolution of plant density is described by a system of partial differential equations (PDEs). Even if the macroscopic models lack information on individual shoots and the rhizome network, they are computationally more efficient to study large systems. Furthermore, bifurcation analysis can be applied to PDEs, providing analytical information about instabilities and tipping points under changing conditions.

Interaction between species is a relevant mechanism in seagrasses dynamics. While some species of seagrasses coexist in space creating mixed meadows, others arrange in separated monospecific beds with interfaces. Some species have been seen in both arrangements for different conditions, suggesting some kind of transition between these behaviors. Interspecies interaction is then key in determining the evolution of ecosystems with invasive species. In a global change scenario like the one we are currently experiencing, the interaction between native species with different responses to the new conditions, *e.g.* due to global warming, can also determine the evolution of the ecosystems [4, 27]. Introducing interspecific interactions to current seagrasses models is necessary to study this process. So far, in the context of seagrass dynamics, interactions between species have only been studied in microscopic models [15, 16]. The addition of interspecies interaction in macroscopic models of seagrasses is, so far, unexplored.

In this work, we present a generalization of a single species seagrass macroscopic model [24] considering local interspecies interaction. Furthermore, we study in detail the bifurcation diagram of the symmetric case, where the two species are similar and the interaction between them is reciprocal. This simple scenario captures the backbone of the general model and, despite its simplicity, it gives a remarkable variety of scenarios with complex behaviors. These scenarios can be related to biotic interactions between species, while the transitions between them are mediated by abiotic (environmental) changes in the mortality rate. General bifurcation scenarios depending on the symmetries of the system can be unraveled making use of normal form theory. This has been done, for instance, in systems with two steady-state mode interactions under O(2)-symmetry [7]. However, although the system considered in this work possess also this symmetry, the former analysis lacks the discrete symmetry associated to the two interacting species.

The ecological implications of the developed model are far-reaching and contribute significantly to our understanding of mixed seagrass meadow dynamics. By incorporating local interspecies interactions into a macroscopic framework, this model allows us to explore how different species of seagrasses coexist, compete, and influence each other's growth patterns within the same habitat. This insight is crucial for predicting the responses of seagrass ecosystems to changing environmental conditions and the potential introduction of invasive species. The model's ability to capture the intricate balance between biotic interactions and abiotic factors, such as mortality rates influenced by environmental changes, sheds light on the mechanisms that underlie transitions between various ecological scenarios. As a result, the model not only enhances our comprehension of complex behaviors within seagrass meadows but also provides valuable guidance for the conservation and management of these critical marine ecosystems. With the looming challenges posed by anthropogenic impacts and global change, the model's insights into interspecies interactions hold the potential to inform targeted restoration efforts and sustainable strategies to ensure the continued vitality of seagrass ecosystems.

2. The model

The first macroscopic model describing the evolution of seagrasses, described in [23], was based on three mechanisms. Firstly, the clonal reproduction of the plant and the production of new shoots are governed by the elongation of the rhizome's end, referred to as the apex. Secondly, the shoots and apices experience a mortality rate that depends on the total plant density. Finally, the rhizome can branch, giving rise to a new apical shoot that grows in a different direction. The branching angle is always approximately the same and

it is a characteristic parameter of the plant species. The resulting model is computationally quite costly as it requires to take into account a field of apex density for each growth direction under consideration.

Such a detailed model can be simplified by a series of assumptions that establish a connection between the density and distribution of apices and the overall plant density field [24]. As a result, the evolution of the total plant density $n(\vec{r}, t)$ can be described by a single partial differential equation:

$$\partial_t n = -n\omega(n) + d_0 \nabla^2 n + d_1((\nabla^2 n)n + ||\nabla n||^2), \tag{2.1}$$

where $\omega(n) = -\omega_b(n) + \omega_d(n)$ is the net death rate, being $\omega_b > 0$ the branching rate and $\omega_d > 0$ the death rate, in principle, both density dependent. The elongation of clonal plant rhizomes, coupled with branching, results in an effective diffusion with coefficient d_0, as well as nonlinear diffusion with coefficient d_1 of the form of $\nabla(n\nabla n)$. In (2.1), we have expanded this nonlinear diffusion term as $\nabla(n\nabla n) = (\nabla^2 n)n + ||\nabla n||^2$.

To describe a two-species system, using equation (2.1), we couple two different vegetation density fields through the mortality term to describe both intraspecific and interspecific interactions:

$$\partial_t n_i = n_i Q_i[\vec{n}] + d_{i0}\nabla^2 n_i + d_{i1}((\nabla^2 n_i)n_i + ||\nabla n_i||^2) \tag{2.2}$$

where we consider local interactions only in the net mortality term, given by a quadratic polynomial:

$$Q_i(\vec{n}) = -\omega_i + \vec{a_i} \cdot \vec{n} - b_{i1}^2 n_1^2 - b_{i2}^2 n_2^2 - b_{i3}n_1 n_2 \tag{2.3}$$

where ω_i is the net mortality of species i in absence of other plants, $\vec{a_i} = (a_{i1}, a_{i2})$, and $\vec{n} = (n_1, n_2)$. a_{ii} and a_{ij} $(i \neq j)$ are the slopes of the linear change in the net mortality rate due to intraspecific and interspecific interactions respectively. A term $a_{ij} > 0$ describes a facilitative interaction for moderate densities while $a_{ij} < 0$ describes a competitive interaction. The quadratic terms $b_{ij} > 0$ are saturation parameters that always describe competitive interactions for high plant densities, acting as a carrying capacity and giving an upper bound to plant density. We will consider the cross saturation terms as $b_{13} = 2b_{11}b_{12}$ and $b_{23} = 2b_{21}b_{22}$, simplifying the mortality term to a cylindric paraboloid form:

$$Q_i(\vec{n}) = -\omega_i + \vec{a_i} \cdot \vec{n} - (\vec{b_i} \cdot \vec{n})^2. \tag{2.4}$$

This way, considering equal interspecific and intraspecific interactions $(\vec{a_1} = \vec{a_2} = (a, a)$ and $\vec{b_1} = \vec{b_2} = (b, b))$, the mortality term is a function of the total density only, *i.e.* the sum of the densities of both species $n_1 + n_2$. This behavior is expected for a homogenous field with a single species, in which different individuals have been labeled in two groups, n_1 and n_2.

The local part of equation (2.2) corresponds to a generalized Lotka-Volterra equation [3, 13] with up to quadratic terms in the mortality rate (2.4), in both inter and intraspecies interactions. The use of these nonlinear interactions is supported by both theoretical and field observations. Specifically, recent studies have shown that interspecific plant–plant facilitation is density dependent and it has a single maximum for intermediate densities [14]. Also, monospecific seagrass meadows show an abrupt collapse of the plant population for small increases of a stressor above a given critical value [17, 18], which indicates the presence of tipping points in the system. Both behaviors need at least up to quadratic nonlinear terms in (2.4) to be properly described.

The obtained model is versatile and can represent species with different growth dynamics. It also allows a flexible representation of the different interactions between plants, such as competition, mutualism, amensalism, or parasitism. Additionally, the model is easily scalable to more than two species, making it a useful tool for studying multispecies seagrass meadows dominant in tropical climates. The plasticity of the model allows for a comprehensive understanding of the complex interactions within ecosystems.

3. The symmetric case

In this section, we consider in detail the simplified case in which both plants are similar and have symmetric interactions, in such a way that the mortality and the intraspecies and interspecies terms are the same for both species, greatly reducing the number of parameters. This implies reciprocal interactions, *i.e.* mutualism and competition are the only possible relationships. For this situation, $\omega_1 = \omega_2 := \omega$, $a_{11} = a_{22} := a_1$, $a_{12} = a_{21} := a_2$, $b_{11} = b_{22} := b_1$, $b_{12} = b_{21} := b_2$, $d_{10} = d_{20} := d_0$, and $d_{11} = d_{21} := d_1$. Notice that, in this symmetric case, $Q_1(n_1, n_2) = Q_2(n_2, n_1) \equiv Q(n_1, n_2)$.

Considering low-density intraspecies facilitation (*i.e.* $a_1 > 0$), the equations can be reduced to an adimensional form through the change of variables

$$n_1' = \frac{b_1^2}{a_1} n_1 \qquad n_2' = \frac{b_1^2}{a_1} n_2 \qquad t' = \frac{a_1^2}{b_1^2} t \qquad \vec{r}' = \frac{a_1}{b_1 \sqrt{d_0}} \vec{r}, \qquad (3.1)$$

and using the following rescaled parameters

$$\omega' = \frac{b_1^2}{a_1^2} \omega \qquad \alpha = \frac{a_2}{a_1} \qquad \beta = \frac{b_2}{b_1} \qquad \delta = \frac{a_1}{b_1^2} \frac{d_1}{d_0}. \qquad (3.2)$$

Dropping the primes, equation (2.2) become:

$$\dot{n_1} = n_1 Q(n_1, n_2) + \nabla^2 n_1 + \delta((\nabla^2 n_1)n_1 + ||\nabla n_1||^2)$$
$$\dot{n_2} = n_2 Q(n_2, n_1) + \nabla^2 n_2 + \delta((\nabla^2 n_2)n_2 + ||\nabla n_2||^2) \qquad (3.3)$$

where

$$Q(n_1, n_2) = -\omega + n_1 + \alpha n_2 - (n_1 + \beta n_2)^2. \qquad (3.4)$$

The new parameter ω is proportional to the net mortality of plants in the absence of interactions. We consider it depends on abiotic factors, *i.e.* it changes with the environmental conditions. Parameters α and β give the ratio between interspecific and intraspecific interactions respectively. Finally, δ is a parameter proportional to the ratio between nonlinear and linear diffusion. In this work, we assume the parameters α, β, and δ not to depend on abiotic factors, and to be determined by the characteristics of the interacting species.

Throughout this work, we fix $\delta = 0.5$ and use α and β as the parameters characterizing the species, and ω as the control parameter whose variations reflect changes in the environment. For fixed biotic parameters (α, β), a change in the value of ω can qualitatively modify the behavior of the system by crossing different bifurcation points. Advancing results to be discussed in detail later, we find that the parameter space (α, β) can be partitioned into ten different regions (see Fig. 1), in each of which the bifurcation diagram as a function of ω is qualitatively different from the others. These ten regions in the parameter space can be further grouped into five different cases (color shaded regions in Fig. 1), each with a different ecological interpretation.

3.1. Homogeneous steady solutions and their bifurcations

The local dynamical system can present up to nine different homogeneous steady states (HSS). These fixed points have been classified into four different groups according to the relative concentration of the different species: one unpopulated P_0; four monospecific P_1^l, P_1^h, P_2^l, P_2^h; two symmetric mixed P_S^l, P_S^h; and two asymmetric mixed P_{A1}, P_{A2} (see Fig. 2). Solutions with a high plant density (labeled with the super-index h) and solutions with a lower plant density (labeled with the super-index l) can be distinguished in the case of symmetric mixed and monospecific HSSs. These solutions can be related by pairs since they are created *via* Saddle-Node bifurcations. Due to the symmetry between species, P_{A1}, P_1^l, and P_1^h have symmetric solutions (P_{A2}, P_2^l, and
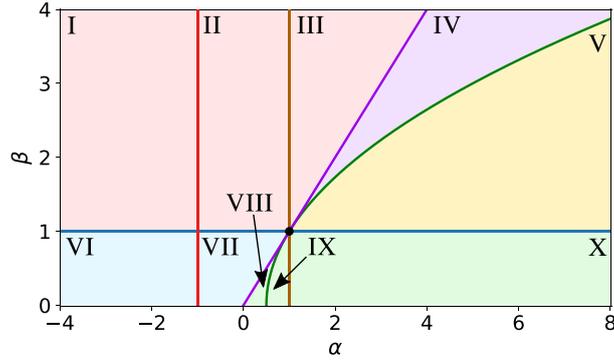
FIGURE 1. Projection of the full phase diagram on the (α, β) plane. Lines represent codimension-2 bifurcations and singular points. These lines divide the interaction parameter plane (α, β) in ten different regions with qualitatively unique bifurcation diagrams as a function of ω, labeled with roman numerals. These regions are grouped into 5 ecological cases: competition exclusion shaded in pink (regions I, II, and III); dynamic coexistence shaded in purple (region IV); low-density coexistence, shaded in yellow (region V); high-density coexistence, shaded in blue (regions VI and VII), and mutualism, shaded in green (regions VIII, IX and X). The red line represents the projection of the codimension-2 bifurcation where SN_S and T_0 cross ($\alpha = -1$); the brown line where $Pitch$ and T_0 cross; the purple line where $Pitch$, SN_S and $Hopf$ converge; and the green curve where T, SN and $Hopf$ converge. Finally, the blue line represents a singular case, $\beta = 1$, where the value of ω at which $Pitch$ and T take place diverges to $-\infty$.
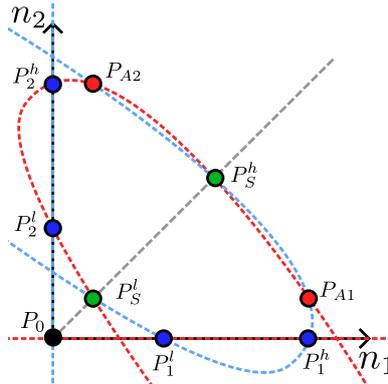

FIGURE 2. Schematic representation of the system's homogeneous steady state (HSS) solutions. The figure shows the nullclines, *i.e.* zero-growth isoclines for the different species, of the local (homogeneous) system. Nullclines for the n_1 (n_2) density are shown in blue (red) dashed lines. Points where the two nullclines cross correspond to fixed points of the local systems, *i.e.* HSSs. There are up to nine of these fixed points, which have been classified into four different groups: unpopulated (black dot), monospecific (blue dots), symmetric mixed states (green dots), and asymmetric mixed states (red dots). Notice the gray dashed symmetry line.

P_2^h) with interchanged plant densities. In the symmetric case considered here, two symmetric solutions are completely equivalent, so from now on we will drop the sub-indices 1 and 2 to refer indistinctly to these solutions, and we will present the results just for the former.

TABLE 1. Homogeneous steady states of equation (3.3). The value of ω_P is given by the critical value of the Pitchfork bifurcation of symmetric state (see Tab. 2).

Label	Name	Value (n_1,n_2)
P_0	Bared state/unpopulated	$(0,0)$
P^h	High populated monospecific	$(0, \frac{1+\sqrt{1-4\omega}}{2}); (\frac{1+\sqrt{1-4\omega}}{2}, 0)$
P^l	Low populated monospecific	$(0, \frac{1-\sqrt{1-4\omega}}{2}); (\frac{1-\sqrt{1-4\omega}}{2}, 0)$
P_S^h	High populated symmetric mixed	$\frac{1+\alpha+\sqrt{(1+\alpha)^2-4\omega(1+\beta)^2}}{2(1+\beta)^2}(1,1)$
P_S^l	Low populated symmetric mixed	$\frac{1+\alpha-\sqrt{(1+\alpha)^2-4\omega(1+\beta)^2}}{2(1+\beta)^2}(1,1)$
P_A	Asymmetric mixed	$\left(\frac{1-\alpha}{2(1-\beta^2)} \pm \sqrt{\frac{\omega_P-\omega}{(1-\beta)^2}}, \frac{1-\alpha}{2(1-\beta^2)} \mp \sqrt{\frac{\omega_P-\omega}{(1-\beta)^2}}\right)$

TABLE 2. Local bifurcations of the HSS.

Label	Name	Critical point ω_c
T_0	Degenerate bared state transcritical	0
SN	Monospecific Saddle Node	0.25
SN_S	Symmetric mixed Saddle Node	$\frac{(1+\alpha)^2}{4(1+\beta)^2}$
T	Monospecific transcritical	$\frac{(1-\alpha)(\alpha-\beta^2)}{(1-\beta^2)^2}$
$Pitch$	Pitchfork of the symmetric state	$\omega_P = \frac{(1-\alpha)(1-3\beta+3\alpha-\alpha\beta)}{4(1-\beta)^2(1+\beta)}$
$Hopf$	Andronov-Hopf of asymmetric mixed state	$\frac{(1-\alpha)(1+2\alpha-2\beta-\beta^2)}{4(1-\beta)^2(1+\beta)}$

The HSSs are created and change their stability through different bifurcations. Plant density values of each HSS and the corresponding bifurcations are listed in Tables 1 and 2 respectively. In Figure 3 we show the ten qualitatively different bifurcation diagrams of the system as a function of ω. These bifurcation diagrams correspond to values of α and β in each corresponding region in Figure 1.

The unpopulated solution, P_0, is a trivial solution of the system which exists for any parameter values. It is stable for $\omega > 0$ and unstable for $\omega < 0$, losing its stability *via* a degenerate (due to the imposed symmetry) transcritical bifurcation, T_0, at $\omega = \omega_c = 0$ involving P^l and either P_S^l or P_S^h. The symmetric mixed state involved in this bifurcation is P_S^h for low values of α (Fig. 3 I and VI) and P_S^l otherwise (Fig. 3 II–V and VII–X). When crossing T_0 changing ω, the involved populated solutions change their sign, having biological relevance only those solutions with positive plant density. Note that the positive HSSs involved in the bifurcation are always unstable close to T_0 due to dominating low-density intraspecies facilitative interaction.

Monospecific solutions P^l and P^h are characterized by the absence of one of the two species. The system can present four of these solutions, two with the absence of n_1 and, equivalently, two symmetric solutions with the absence of n_2. These fixed points are generated in two simultaneous monospecific-Saddle-Node (SN) bifurcations. The higher branch of the SN corresponds to P^h, stable under density perturbations of the same species, while the lower branch corresponds to P^l, which is always unstable.

For a single species the system shows the so-called Allee effect, a positive correlation between the growth rate and the population size for small densities [6]. For $\omega > 0$, the Allee effect is strong, and there is a threshold (given by P^l) below which the plant density decays. The system can show bistability between the unpopulated, P_0, and the higher populated monospecific solutions, P^h, in this regime. For $\omega < 0$, the system displays a weak Allee effect, *i.e.* there is no threshold for the growth of plant density. Thus, in this regime, P^h will be stable and P_0 unstable, while P^l is negative and does not have a biological meaning in this context. The transition between these two regimes, *i.e.* between monospecific strong and weak Allee effect, occurs through the already discussed transcritical bifurcation T_0, involving P_0 and P^l.
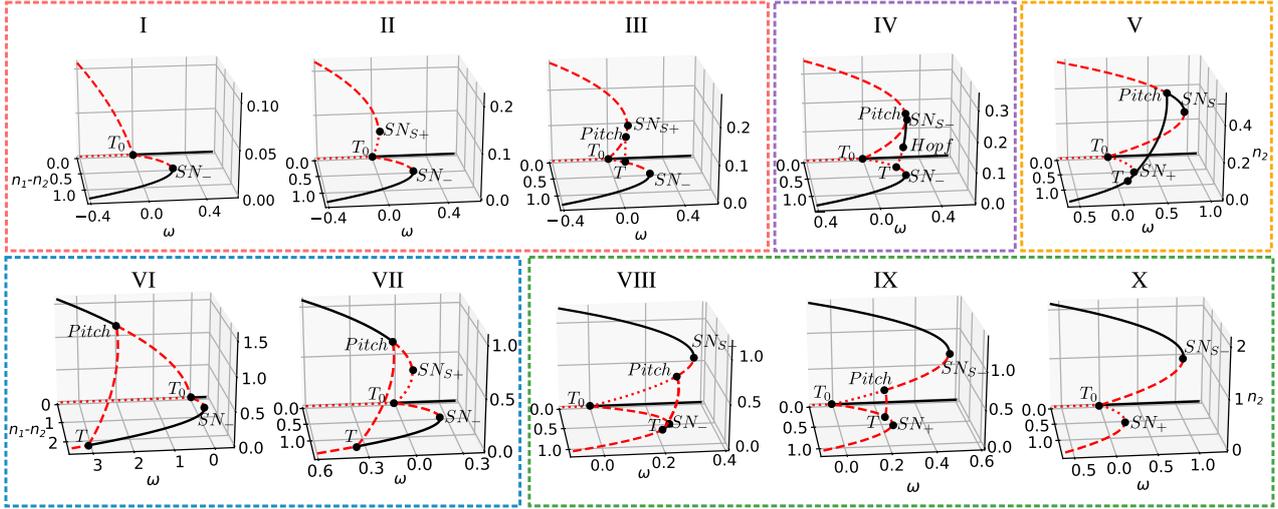
FIGURE 3. Bifurcation diagram as function of the mortality ω in the different regions shown in Figure 1. The x-axis represents the difference between the population of the two different species, $n_1 - n_2$, the z-axis represents the density of species 2, n_2, and the y-axis represents the control parameter ω. The branch on the y-axis ($n_2 = 0$ and $n_1 - n_2 = 0$) corresponds to P_0 (black dot in Fig. 2); branches on the x–y plane ($n_2 = 0$) correspond to P^l and P^h (blue points in Fig. 2), branches on the y–z plane ($n_1 - n_2 = 0$) correspond to P_S^l and P_S^h (green points in Fig. 2), and branches out of these planes correspond to P_A (red points in Fig. 2). Asymmetric mixed steady states with a concentration of n_2 higher than n_1 and monospecific states with species 1 are not shown but, due to the symmetry of the system, these solutions have the same bifurcation diagram as the equivalent solutions shown here. Solid black lines represent stable fixed points, red dashed lines saddle points, and red dotted lines unstable nodes or spirals. Colored squares around the diagrams group them into the five different ecological frameworks. The numbers and colors match those used in Figure 1.

When considering the presence of the other species, the stability of the higher populated monospecific state, P^h, is not guaranteed. In regions I–IV and VI–VIII, P^h is stable right from the SN, which corresponds to a SN_- of the local system. Otherwise, in regions V, IX, and X, the SN corresponds to a SN_+, and P^h is unstable to perturbations consisting of a small population of the other species. Away from SN, P^h can still change its stability through a secondary transcritical bifurcation (T) with P_A, see for instance Figure 3 V and VI–VIII. Crossing this bifurcation point, by decreasing ω, P_A enters a quadrant of negative values, losing its biological meaning. On the other hand P^h changes its stability, either losing it in a catastrophic transition (see Fig. 3 VI–VIII) or gaining it (Fig. 3 V).

Symmetric mixed solutions (P_S^h and P_S^l) are characterized by having the same population of both species, $n_1 = n_2$. These solutions are generated at a saddle-node bifurcation with symmetric plant concentrations (SN_S). By decreasing ω to 0, either P_S^h or P_S^l, will interact with P_0 in T_0 changing its sign. In contrast with the monospecific saddle node (SN), which occurs always for positive densities, as low densities intraspecific facilitation is assumed in this work, the SN_S might occur for negative population values (see Fig. 3 I and VI), and therefore the solutions have no biological meaning at the bifurcation. When this happens (regions I and VI), P_S^h interacts with P_0 at T_0, becoming positive for $\omega < 0$, while P_S^l takes always negative values in this case.

When SN_S occurs for positive density values, *i.e.* in regions II–V and VII–X (see Fig. 3), two different scenarios are found when considering the stability of P_S^h at the bifurcation point. On one hand, P_S^h is stable at the bifurcation point in regions IV, V, and VIII–X; where we label the SN_S bifurcation as SN_{S-}. On the other

hand, P_S^h is unstable at the bifurcation in regions I–III, VI, and VII; where we denote the SN_S bifurcation as SN_{S+}.

A symmetric mixed solution, either P_S^h or P_S^l, is also involved in a Pitchfork bifurcation ($Pitch$), *i.e.* a spontaneous symmetry breaking of the system, from where a pair of asymmetric mixed solutions (P_A) emerges. Depending on the region, this bifurcation affects one branch or the other of P_S (see Fig. 3). In regions I, II, and X, $Pitch$ involves P_S^l but for negative values; and P_A does not have biological meaning for any value of ω. In regions III, VIII, and IX, $Pitch$ involves P_S^l with positive values. In regions IV, V, VI, and VII $Pitch$ affects P_S^h, changing the stability of this point. In this last case, we can make a relevant distinction. In regions IV and V $Pitch$ is supercritical and P_A is stable after the bifurcation, while in regions VI and VII $Pitch$ is subcritical and P_A is unstable. Moreover, in region IV, P_A undergoes a Andronov-Hopf bifurcation ($Hopf$), where the stability of P_A changes by decreasing ω before reaching the T bifurcation. After the Hopf bifurcation a stable homogeneous limit cycle with densities oscillating around P_A is observed. The dynamics of the limit cycle will be discussed in Section 4.1.2.

The regions in the (α, β) parameter space where each archetypal bifurcation diagram is found are shown in Figure 1. The curves separating the different regions are given by the projection of codimension-2 bifurcations and singular parameter values of the complete four dimensional parameter space on the (α, β) plane. Regions I and II, and VI and VII are separated by the a codimension-2 bifurcation point in which SN_S and T_0 occur for the same parameter values, shown as a red line at $\alpha = -1$ in Figure 1. Regions II and III, and IX and X are separated by the codimension-2 bifurcation in which T_0, T, and $Pitch$ occur for the same parameter values, shown as a brown line at $\alpha = 1$ in Figure 1. Regions III and IV, and VII and VIII are separated by the codimension-2 bifurcation in which $Pitch$ and SN_S occur for the same parameter values, marked as a purple line in Figure 1 ($\alpha = \beta$). This codimension-2 point, in the case separating regions III and IV, also involves $Hopf$ and a Double Heteroclinic (DH) bifurcation, in a Bogdanov-Takens bifurcation. The DH global bifurcation is introduced in more detail in Section 4.1.2. The separation between regions IV and V, and VIII and IX are given by the codimension-2 point in which T, $Pitch$, and $Hopf$ occur for the same parameter values, marked in green in Figure 1 ($2\alpha = (1 + \beta)^2$). Finally, the blue line in Figure 1, separating regions I, II, and V from VI, VII, and X respectively, represents a singular point in the (α, β) subspace, given by $\beta = 1$. Approaching this value of β, the critical value of ω at which the bifurcations affecting P_A occur, *i.e.* $Pitch$ and T, diverges to $-\infty$.

4. Interaction scenarios

The structure of the HSS bifurcation diagram as a function of the net mortality rate ω changes depending on the values of inter/intra-species interaction ratios (α, β), as shown in Figures 1 and 3. Nevertheless, some of these regimes differ in bifurcations affecting only unstable HSS or involving solutions with negative density values. Therefore, we can group the ten cases into just five scenarios with significantly different behavior and ecological interpretation. The regions encompassed in each scenario are shaded with the same color in Figure 1 and grouped by dashed-line boxes in Figure 3. We further classify the 5 scenarios in two cases: scenarios for large saturation ratios ($\beta > 1$) and scenarios for small saturation ratios ($\beta < 1$).

4.1. Scenarios for large saturation ratios ($\boldsymbol{\beta > 1}$)

In this section we study the large-saturation-ratio case, *i.e.* $\beta > 1$, meaning that the interspecific saturation term is larger than the intraspecific one. Therefore, in this region of the parameter space monospecific meadows are favored, especially for the large densities appearing for small mortality rates. Nevertheless, for intense interspecific facilitation (large values of α) stable mixed meadows (either P_S^h or P_A) can appear for intermediate mortality rates, as well as more exotic behaviors such as oscillations or excitability, due to strongly nonlinear dynamics.
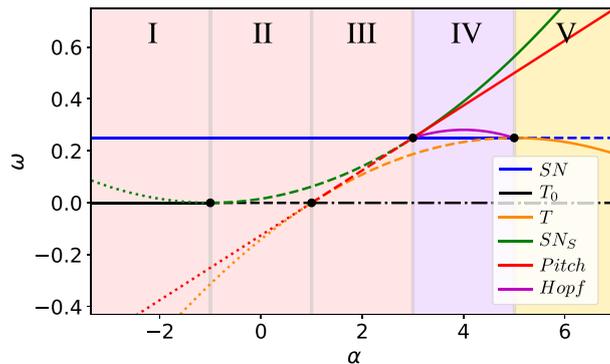
FIGURE 4. (α, ω) phase diagram for $\beta = 3$, crossing through regions I–V in Figure 1. This phase diagram is representative of any configuration with $\beta > 1$. Dotted lines represent bifurcation involving negative steady points, *i.e.* solutions without physical meaning. The blue line represents SN, solid (dashed) when it corresponds with SN_- (SN_+). The green line represents SN_S, solid (dashed) when it corresponds with SN_{S-} (SN_{S+}). The red solid (dashed) line represents the supercritical (subcritical) pitchfork bifurcation from where P_A emerges. The orange solid (dashed) line represents T involving P^h (P^l). The black line represents T_0, solid when involving P_S^h, and dashed (dot-dashed) when involving P_S^l as an unstable node (saddle). Finally, the purple line represents the supercritical $Hopf$ of P_A. Dots mark the codimension-2 points. Roman numerals indicate the regions shown in Figures 1 and 3, while the shaded colors mark the different ecological cases.

A representative phase diagram of this region in the (α, ω) parameter space is shown in Figure 4 for $\beta = 3$. We next discuss the three different dynamical regimes in this scenario.

4.1.1. Competitive exclusion scenario

For $\alpha < \beta$ (regions I, II, and III; pink shaded in Fig. 1), there are no stable mixed states. In this scenario, plants compete with each other for all plant densities. Representative bifurcation diagrams are shown in Figure 3 I–III.

For mortality values above the saddle-node bifurcation of the monospecific solutions SN (*i.e.* $\omega > 0.25$) the only possible state of the system is bare soil (P_0), to which any initial condition will converge. For $\omega \in (0, 0.25)$ the system shows bistability. On one hand, P_0 is still stable, and not dense enough initial conditions die out (strong Allee effect). On the other hand, P^h, with either one or the other species, is stable, and dense enough initial conditions will form monospecific meadows. Here P^l acts as a critical density below which the system goes to bare soil and above which the system develops a meadow. For lower moralities ($\omega < 0$), the system tends always to monospecific solutions (weak Allee effect).

In this scenario the system displays a hysteresis cycle; the system has a tipping point at $\omega = 0.25$ where the populated solution collapses to the bare state. On the other hand, at $\omega = 0$, P_0 destabilizes and for $\omega < 0$ each species may grow at different places, forming domains separated by fronts. Typically the system shows curvature driven coarsening, in such a way that closed domains will tend to a circular shape and shrink, following its size a $t^{1/2}$ scaling law, until disappearing completely [10]. In this case, the final state at long times is always either a single species meadow or regions of different species separated by flat fronts, similar to Figure 5a–h. This phase separation scenario can be related to dominating competitive ecological interactions between species. This situation is structurally unstable, and any breaking of the symmetry between species will make the dominant one to overrun the other and colonize all the space.
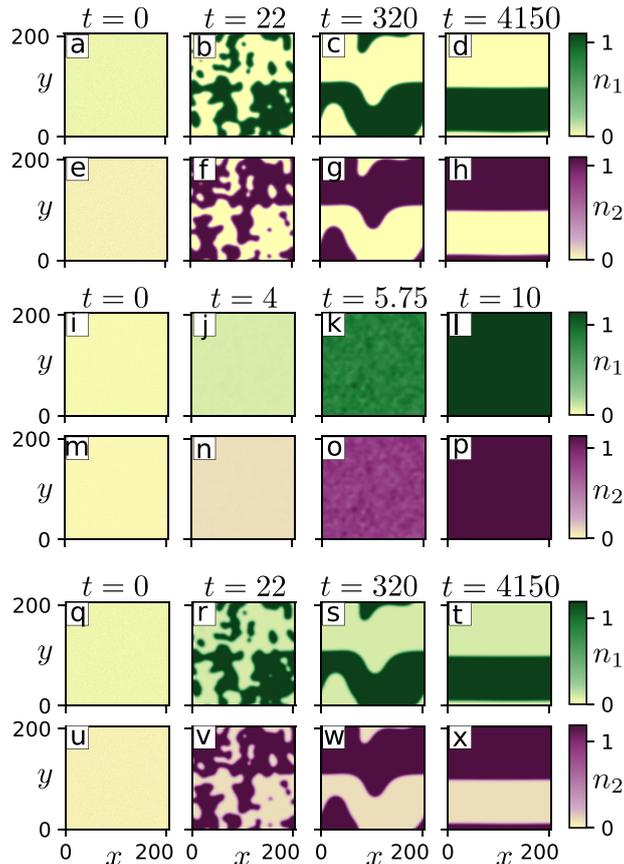
FIGURE 5. Numerical simulation after the T_0, for $\omega = -0.1$. The simulations are initialized around P_0 with an additional small Gaussian noise and are performed on a squared domain with periodic boundary conditions. The panels show frames of the density fields for n_1 (a–d, i–l, and q–t) and n_2 (e–h, m–p, and u–x). The simulation has been performed for three different parameter configurations, showing the 3 different transitions when crossing the bifurcation point. Panels a–h show phase separation to P^h (with $P^h \approx (1.09, 0); (0, 1.09)$), for $\alpha = 5$ and $\beta = 2.5$. Panels i–p show the transition to P_S^h (with $P_S^h \approx (1.13, 1.13)$), for $\alpha = 6$ and $\beta = 1.5$. Panels q–x show phase separation to P_A (with $P_A \approx (1.18, 0.09); (0.09, 1.18)$), for $\alpha = 7.7$ and $\beta = 2.5$.

4.1.2. Strongly nonlinear regime

The region with $\beta < \alpha < \frac{1}{2}(1 + \beta^2)$ (region IV, shaded in purple in Fig. 1) presents a highly nonlinear behavior for intermediate values of mortality. This behavior is generated due to the interplay between strong quadratic interspecies facilitation terms and also strong cubic interspecies saturation.

As usual, for large enough mortality rates, the only possible final state of the system is P_0, and any initial non-zero population decays. For lower mortality values, the system shows bistability between P_0 and P_S^h. However, for smaller mortality values, P_S^h destabilizes through a supercritical pitchfork bifurcation, leading to a phase separation dynamics of the two asymmetric solutions P_A, similar to the one shown in Figure 6i–p. For even lower mortalities, P_A undergoes a Hopf bifurcation and densities n_1 and n_2 oscillate around these states.

The dynamics of the limit cycle for decreasing values of ω is shown in Figure 7. Decreasing ω, the limit cycle growths in amplitude and approaches P_S^l and P_S^h simultaneously (see Fig. 7a, b and c). Close to these
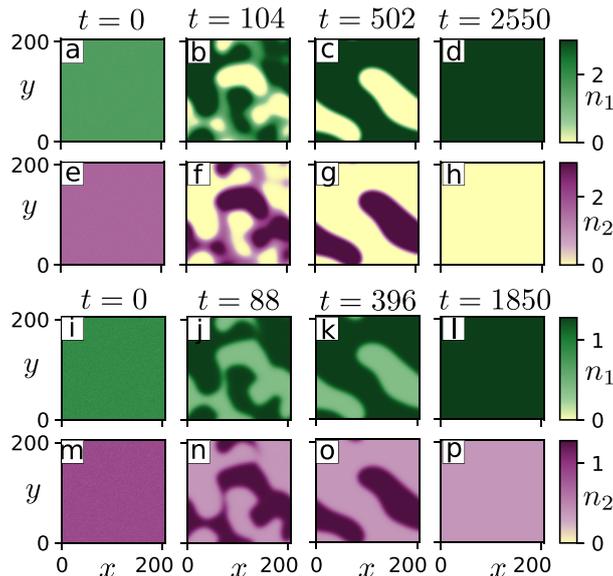
FIGURE 6. Numerical simulations close to $Pitch$ bifurcation. The simulations are initialized around P_S^h with a small Gaussian noise and performed on a square lattide with periodic boundary conditions. The panels show frames of the density fields for n_1 (a–d and i–l) and n_2 (e–h and m–p). The simulation has been performed for two different parameter configurations, one showing the behavior after the subcritical $Pitch$ (a–h), with $\omega = -6.04$, $\alpha = -2$, and $\beta = 0.3$, where the system shows a a separation to P^h solutions (with $P^h \approx (3.01, 0); (0, 3.01)$); and the other after the supercritical $Pitch$ (i–p), with $\omega = -0.616$, $\alpha = 6$, and $\beta = 2$, where the system shows a separation to P_A solutions (with $P_A \approx (1.28, 0.39); (0.39, 1.28)$).

fixed points, the limit cycle slows down (see Fig. 7e and f). Eventually, decreasing ω even more, the limit cycle touches P_S^l and P_S^h in a Double-Heteroclinc connection (DH), as shown in Figure 7c). After this bifurcation point, the limit cycle is destroyed and the local system presents Type-I excitable behavior (see Fig. 7d and g).

In this excitable regime, homogeneous initial conditions below a threshold, given by the stable manifold of P_S^l, decay to the bare state. Homogeneous initial conditions above this threshold will, however, make a large excursion in phase space to finally come back to the bare state again, an excitable trajectory (see Fig. 7d and g). This leads to the apparent paradoxical absence of persistent populated solutions in the so called "excitable regime". This paradoxical behavior can be related to the "enrichment paradox" [22] observed in many population dynamics models. However, in this case, localized initial conditions grow in this regime, creating a turbulent state that expands onto bared soil. An example of this regime is shown in Figure 7h–o. At difference with other models [1, 19], for the parameters used in this study we have not observed stable travelling pulses in the excitable regime, only turbulent states.

4.1.3. Obligate mutualism to monospecific transition

For $\alpha > \frac{1}{2}(1 + \beta^2)$ (region V, shaded in yellow in Fig. 1) we observe a smooth transition from mixed symmetric, P_S^h, to monospecific, P^h, meadows through asymmetric states, P_A (see panel V in Fig. 3). This transition can be understood as an obligate mutualism interaction for low plant densities, but a competitive interaction for high densities, giving rise to a competitive exclusion scenario for small mortalities.

In this scenario, the system presents a hysteresis cycle between populated solutions and P_0. For high mortality, P_0 is the only possible state. Decreasing the mortality the system crosses SN_S, after which it shows bistability between P_0 and P_S^h. If we follow the populated branch P_S^h while decreasing ω, there is a point where the system
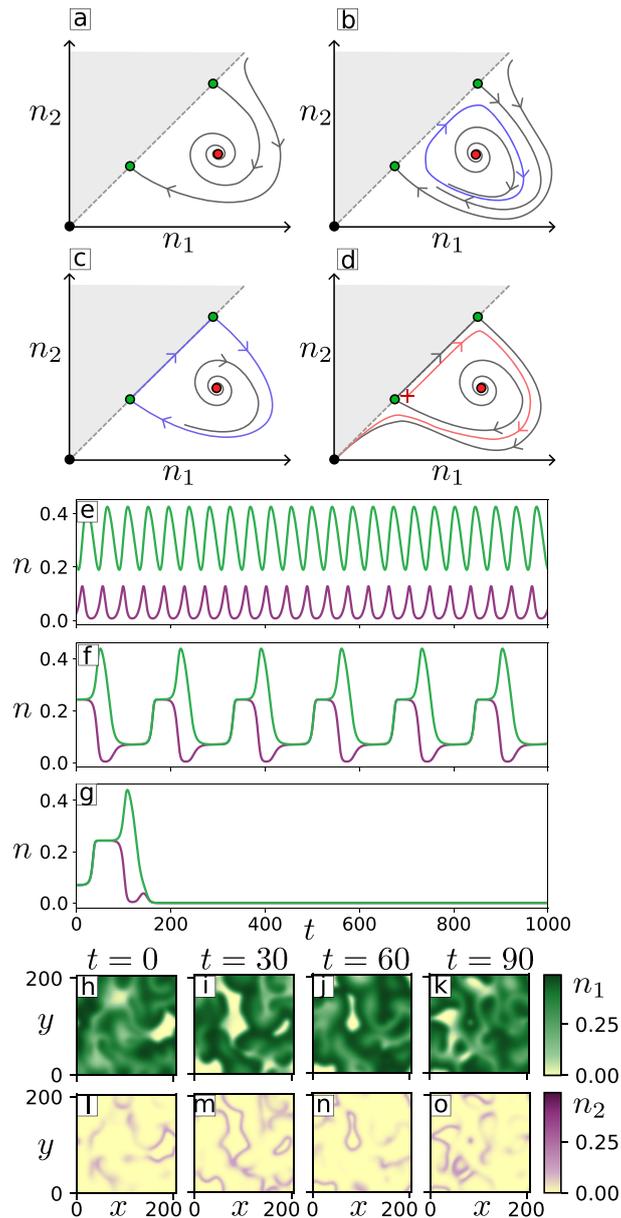
FIGURE 7. Oscillatory and turbulent regimes around asymmetric solutions. Panels a)-d) show sketches of the phase diagram for different values of ω in region V: a) between $Pitch$ and $Hopf$; b) after the $Hopf$, P_A destabilizes and a stable limit cycle emerges. Decreasing ω further, the limit cycle grows in amplitude and approaches P_S^h and P_S^l, until it touches them, c), at a double heteroclinic (DH). Approaching this bifurcation point, the period of the oscillations diverges and the limit cycle is destroyed after crossing it. After this point, the system shows local excitability, see red trajectory in panel d). Panels e)-g) show the time evolution of each species density in the oscillatory regime for $\alpha = 4$ and $\beta = 3$, and (e) $\omega = 0.275$ far from the DH bifurcation, (f) $\omega = 0.27082$ closer to DH, and (g) $\omega = 0.27$ in the excitable regime passed the DH. Panels h)-o) show the turbulent regime observed in the excitable region for $\omega = 0.251$ with periodic boundary conditions.
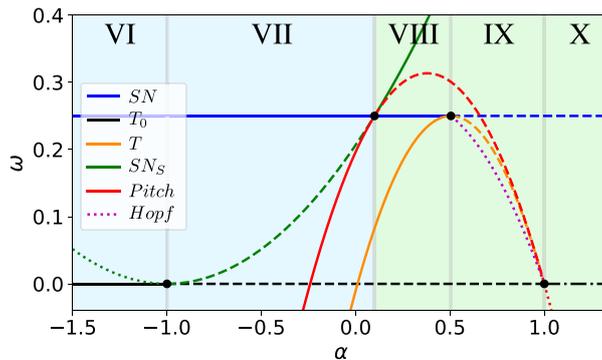
FIGURE 8. Phase diagram for $\beta = 0.1$ crossing through regions VI–X. This phase diagram is representative of any configuration with $\beta < 1$. Dotted lines represent bifurcation involving negative steady points, *i.e.* solutions without physical meaning. The blue solid (dashed) line represents the SN_- (SN_+) bifurcation. The green line represents the SN_S, solid (dashed) when corresponding to SN_{S-} (SN_{S+}). The red solid (dashed) line represents the subcritical (supercritical) *Pitch* involving P_S^h (P_S^l). The orange solid (dashed) line represents T involving P^h (P^l). The black line represents T_0, solid when involves P_S^h, dashed when involves P_S^l while it is a node, and dotted-dashed when involves P_S^l while it is a saddle. The purple dotted line represents the *Hopf* bifurcation of P_A, with negative density values. Dots mark the codimension-2 points. Roman numerals indicate regions shown in Figures 1 and 3, while the shaded colors mark the ecological cases.

eventually crosses a supercritical pitchfork bifurcation (*Pitch*) and P_S^h loses stability. Initial conditions around P_S^h slightly below this point tend to phase separate driven by curvature, forming domains of either one of the two assymmetric solutions, P_{A1} or P_{A2}, as shown in Figure 6i–p. Decreasing ω even more, P_A becomes more and more asymmetrical, one of the two species increasing its density while the other decreases it until P_A eventually reaches P^h in T. This gives a continuous transition of the populated stable solutions from P_S^h to P^h while decreasing ω.

Here the stable bare state coexists with stable populated solutions (either P_S^h, P_A or P^h) until $\omega = 0$ where it loses its stability through T_0. Crossing this threshold, the system undergoes a phase separation involving either the monospecific solutions (see Fig. 5a–h) or the asymmetric mixed solutions (see Fig. 5q–x), depending on the relative position of *Pitch* and T due to the parameter values.

4.2. Scenarios for small saturation ratio ($\boldsymbol{\beta < 1}$)

In this section, we study the scenarios with a small saturation ratio, *i.e.* when $\beta < 1$ and therefore the intraspecies saturation is greater than the interspecies one. In this region of parameter space, the P_S^h is favored, especially for small mortality values where it shows large densities. Nevertheless, for small values of the parameter α, describing interspecies competition or just very weak interspecies facilitation for low plant densities, the system can also show monospecific meadows for intermediate mortalities.

A representative phase diagram of this region in the (α, ω) parameter space is shown in Figure 8 for $\beta = 0.1$. We next discuss the two different cases in this scenario.

4.2.1. Competitive exclusion to facultative mutualism transition

For small values of α, *i.e.* $\alpha < \beta$ (regions VI and VII, blue shaded in Fig. 1), the system tends to P^h for intermediate mortality values, and to P_S^h for lower mortalities. The transition between these two configurations is abrupt, and the system shows a hysteresis cycle. This hysteresis cycle coexists with another one between populated and unpopulated solutions (see Fig. 3VI–VII).

The transition from monospecific, P^h, to mixed symmetric, P_S^h, meadows occurs through T, that involves the (unstable) P_A. The transition from P_S^h to P^h occurs after a subcritical pitchfork, $Pitch$. This transition leads to a spontaneous symmetry breaking and a phase separation of the two monospecific solutions (see Fig. 6a–h).

The populated-unpopulated hysteresis cycle involves P^h, which is destroyed at SN for $\omega = 0.25$. For larger mortalities, any initial condition decays to the bared state P_0. P_0 is stable above T_0. After this bifurcation, and depending on the parameters, the system can show a phase separation to P^h (similar to Fig. 5a–h) or converge to P_S^h (similar to Fig. 5i–p).

4.2.2. Obligate and facultative mutualism

For large values of α, *i.e.* $\alpha > \beta$ (regions VIII, IX, and X, shadowed in green in Fig. 1), P_S^h is always stable below SN_s. Representative bifurcation diagrams of this region are shown in Figure 3 VIII, IX and X.

For large mortality values, the symmetric mixed solution has a tipping point (SN_s) and the system collapses to the bare state. This bare state coexists with the symmetric mixed solution until $\omega = 0$, after which the system converges to the symmetric mixed solution (similar to Fig. 5i–p).

In region VIII there is a small set of mortality values for which the monospecific solution is also stable, showing the system bistability between monospecific and symmetric mixed populated states.

5. Conclusions

We have presented a general spatiotemporal population dynamics model for two interacting seagrass species. The interaction between species has been introduced as a coupling through the mortality rate, with up to quadratic density dependent terms. This allows modeling of different types of interactions. Regarding intraspecific interactions, these nonlinear terms allow low-density facilitation and high-density saturation leading to bounded solutions, *i.e.* Allee effect. For the interspecific interactions, the nonlinear density dependence allows, for some parameters, the prevalence of monospecific solutions, and species segregation for large densities associated to low mortality rates. This density-dependent interspecific interaction, which has been experimentally observed in other plant species [14], has nontrivial landscape effects. The system includes also non-linear diffusion and a gradient squared term to model clonal reproduction. This model allows us to delve into the intricacies of species coexistence, competition, and mutual influence within a shared habitat.

The core of our investigation has revolved around the symmetric scenario, where species interactions are equal and reciprocal. Within this framework, the system parameters are reduced to just 4 in its adimensional form. By analyzing the bifurcation diagram, we have constructed a foundational understanding of this symmetric scenario, which serves as the backbone for the general case.

Notably, our exploration of the parameter space has unveiled ten distinct regions, each delineated by the values of the biotic parameters α and β, governing the balance between intraspecific and interspecific interactions. These regions exhibit qualitatively distinct bifurcation diagrams in response to changes in the net mortality rate ω, a parameter tied to abiotic factors. Furthermore, we have grouped these regions into five distinct ecological scenarios, ranging from obligate and facultative mutualism to competitive exclusion and strongly nonlinear regimes. Our analysis underscores the remarkable diversity of dynamics achievable within this model, including phenomena such as stable symmetric and asymmetric states, oscillations, turbulence, and competitive exclusion. The system shows, for some parameter ranges, abrupt transitions between these dynamics, compatible with the field observations on seagrasses meadows [17, 18].

Some of these scenarios (regions VI–X in Fig. 1) are compatible with a linear interaction between species, corresponding in the model to $\beta = 0$. Nevertheless, some of the dynamics found in regions I–V are incompatible with just lineal interspecific interaction in a symmetric system. These dynamics include stable asymmetric states, oscillations, turbulence, and competitive exclusion.

While our detailed investigation has been centered on the symmetric case, we recognize that real-world scenarios often involve asymmetric interactions between species. Therefore, a natural extension of our work

lies in its application to specific cases, mirroring the approach taken with microscopic seagrass models and single-species macroscopic systems in previous studies [15, 16, 23].

The ecological relevance of our model is profound, as it offers fresh insights into the dynamics of seagrass meadows. By embracing local interspecies interactions within a macroscopic framework, our model empowers us to unravel the complex tapestry of coexistence, competition, and the interplay of biotic and abiotic influences. These revelations are pivotal for anticipating how seagrass ecosystems might respond to evolving environmental conditions and the potential intrusion of invasive species. Moreover, our model's adeptness at capturing the delicate equilibrium between species interactions and mortality rates shaped by the environment casts light on the mechanisms underpinning shifts between different ecological scenarios.

In conclusion, our research not only enriches our comprehension of the complexities within seagrass meadows but also contributes to the broader field of ecological modeling. In a landscape where human activities and global changes pose formidable challenges, the insights gleaned from our model's exploration of interspecies dynamics have the potential to guide targeted restoration endeavors and sustainable strategies.

Appendix A. Linear stability analysis.

In this appendix, we describe the stability analysis used to study the bifurcations affecting HSSs. In particular, we show that there are no finite wavelength instabilities, a.k.a. Turing instabilities, for any of these solutions.

To study the linear stability of HSSs we consider small perturbations of the form:

$$\vec{n}_q = \vec{n}_q^0 e^{\sigma_q t + iqx} \tag{A.1}$$

where σ_q is the eigenvalue associated with the eigenvector $\vec{n}_q^0$ of the Jacobian matrix around the HSS:

$$J_q(n_1^*, n_2^*) = J_0(n_1^*, n_2^*) + \begin{pmatrix} -(1 + \delta n_1^*)q^2 & 0 \\ 0 & -(1 + \delta n_2^*)q^2 \end{pmatrix} \tag{A.2}$$

where J_0 is the homogeneous Jacobian matrix, given by:

$$J_0(n_1^*, n_2^*) = \begin{pmatrix} J_{11} & J_{12} \\ J_{21} & J_{22} \end{pmatrix} = \begin{pmatrix} Q(n_1^*, n_2^*) + n_1^* - 2n_1^*(n_1^* + \beta n_2^*) & n_1^*[\alpha - 2\beta(n_1^* + \beta n_2^*)] \\ n_2^*[\alpha - 2\beta(n_2^* + \beta n_1^*)] & Q(n_2^*, n_1^*) + n_2^* - 2n_2^*(n_2^* + \beta n_1^*) \end{pmatrix} \tag{A.3}$$

The bifurcations presented in this paper can straightforwardly be obtained through the study of the eigenvalues of the J_0 matrix.

To detect pattern forming instabilities one must consider the full Jacobian $J_q(n_1^*, n_2^*)$. Although in the symmetric case the diffusion coefficients are equal, $d_{10} = d_{20}$, the presence of nonlinear diffusion does not allow to discard, *a priori*, the presence of a Turing instability in the system. In what follows, however, we prove that, despite nonlinear diffusion, no Turing instability can take place in the symmetric case for any of the HSSs.

Six different conditions must be fulfilled in order to a Turing instability to take place. First, both field of the homogeneous solution must be positive to have physical meaning:

$$n_{1,2}^* \geq 0. \tag{A.4}$$

Second, the solution might be linearly stable under homogeneous perturbation, and therefore following two conditions must be fulfilled:

$$\tau = J_{11} + J_{22} < 0 \tag{A.5}$$

$$\Delta = J_{11}J_{22} - J_{12}J_{21} > 0. \tag{A.6}$$

Finally, the transition must happen for a real critical wavenumber and a positive value of the control parameter δ:

$$q_c^2 = \frac{J_{11}(1 + \delta n_2^*) + J_{22}(1 + \delta n_1^*)}{2(1 + \delta n_1^*)(1 + \delta n_2^*)} > 0 \tag{A.7}$$

$$\delta_c > 0. \tag{A.8}$$

A.1 Turing of the unpopulated solution

In this subsection, we prove that the unpopulated solution has no physically meaningful Turing instability.

First, the growth of a non-zero-wavenumber perturbation on top of the bare state implies regions of the space with a negative value of the population density of at least one species. These solutions, therefore don't have physical meaning and are forbidden, by construction, on the system.

Nevertheless, we can compute the square critical wavenumber q_c^2 equation to obtain, $q_c^2 = -\omega$. Therefore this critical wavenumber only exists for negative values of ω. Computing the determinant and the trace of the linearized system for perturbations with q_c, we obtain $\tau_c = 0$ and $\Delta_c = 0$, showing that the value at this point does not depend on δ, meaning that the eigenvalue associated with q_c will be a double geometric-degenerated zero and never will be positive. This point, therefore, is not associated with a Turing instability but is a consequence of the symmetries of the problem.

A.2 Turing of the monospecific solutions

In this subsection, we prove that there is no physically meaningful Turing instability for monospecific homogeneous solutions. As the matrix given by equation (A.2) is triangular, the eigenvalues are easily obtained for the $P^{l,h}$. Their eigenvalues are given by the following equation:

$$\lambda_1(q) = n^* - 2n^{*2} - (1 + \delta n^*)q^2$$
$$\lambda_2(q) = -\omega + \alpha n^* - \beta^2 n^{*2} - q^2 \tag{A.9}$$

where n^* is the plant density of the populated specie. The only relative maximum of both eigenvalues is for $q = 0$ and, therefore, no Turing instability can take place for monospecific HSSs.

A.3 Turing of the symmetric mixed solution

Using equations (A.5) and (A.7) for $P_S^{l,h}$ we obtain:

$$q_c^2 = \frac{\tau}{4(1 + \delta n_i^*)}. \tag{A.10}$$

Assuming conditions (A.4), and (A.8) are fulfilled, we obtain that $q_c^2 > 0 \iff \tau > 0$, which contradicts either condition (A.5) or (A.7). Therefore it is not possible to fulfill all the conditions at the same time and there is no Turing instability for symmetric mixed solutions.

A.4 Turing of asymmetric mixed solutions

To work with asymmetric mixed solutions we will make use of the following change of variables: $\mu = n_1 + n_2$, $\nu = n_1 - n_2$. The asymmetric mixed solution is given by $\mu^* = \frac{1-\alpha}{1-\beta^2}$ and $\nu^* = \pm 2\sqrt{\frac{\omega_P - \omega}{(1-\beta)^2}}$. Notice that condition (A.4) is only fulfil when $|\nu^*| < \mu^*$ and $\mu^* > 0$.

With this change of variables, condition (A.5) reads:

$$\tau = \mu^*(1 - \mu^* - \beta\mu^*) - \nu^{*2}(1 - \beta) < 0. \tag{A.11}$$

While, assuming conditions (A.4) and (A.8) are fulfilled, we can focus just in the numerator of (A.7) and rewrite it as:

$$\tau + \delta(J_{11}n_2^* + J_{22}n_1^*) > 0. \tag{A.12}$$

As $\tau < 0$, a necessary but not sufficient condition for this last inequality is:

$$J_{11}n_2^* + J_{22}n_1^* = \frac{1}{2}(\mu^{*2} - \nu^{*2})(1 - \mu^* - \beta\mu^*) > 0, \tag{A.13}$$

and,as $|\nu^*| < \mu^*$, this condition reduces to $1 - \mu^* - \beta\mu^* > 0$, or, as $\beta > 0$, to $\mu^* < \frac{1}{1+\beta}$.

Substituting this last expression on (A.11), assuming $\mu^* > 0$, we arrive to the necessary condition $\beta < 1$. Now, from the same expression and considering again $|\nu^*| < \mu^*$ we arrive to to:

$$\mu^*(1 - \mu^* - \beta\mu^*) < \nu^{*2}(1 - \beta) < \mu^{*2}(1 - \beta) \tag{A.14}$$

and therefore:

$$\mu^* > \frac{1}{2}. \tag{A.15}$$

Altogether we get $\frac{1}{2} < \mu^* < \frac{1}{1+\beta} < \frac{1}{2}$, wich has no solution. Therefore we conclude that there is no Turing instability of the asymmetric solutions.

References

[1] A. Arinyo-i Prats, P. Moreno-Spiegelberg, M.A. Matias and D. Gomila, Traveling pulses in type-I excitable media. *Phys. Rev. E* **104** (2021) L052203.

[2] M.W. Beck, K.L. Heck, K.W. Able, D.L. Childers, D.B. Eggleston, B.M. Gillanders, B. Halpern, C.G. Hays, K.Hoshino, T.J. Minello, R.J. Orth, P.F. Sheridan and M.P. Weinstein, The identification, conservation, and management of estuarine and marine nurseries for fish and invertebrates. *Bioscience* **51** (2001) 633–641.

[3] L. Brenig, Complete factorization and analytic solutions of generalized lotka-volterra equations. *Phys. Lett. A* **133** (1988) 378–382.

[4] C.J. Collier, S. Uthicke and M. Waycott, Thermal tolerance of two seagrass species at contrasting light levels: implications for future distribution in the Great Barrier Reef. *Limnol. Oceanogr.* **56** (2011) 2200–2210.

[5] R. Costanza, R. D'Arge, R. de Groot, S. Farber, M. Grasso, B. Hannon, K. Limburg, S. Naeem, R.V. O'Neill, J. Paruelo, R.G. Raskin, P. Sutton and M. van den Belt, The value of the world's ecosystem services and natural capital. *Nature* **387** (1997) 253–260.

[6] F. Courchamp, L. Berec and J. Gascoigne, Allee Effects in Ecology and Conservation. OUP, Oxford (2009).

[7] G. Dangelmayr, Steady-state mode interactions in the presence of 0(2)-symmetry. *Dyn. Stabil. Syst.* **1** (1986) 159–185.

[8] C. M. Duarte, J. J. Middelburg and N. Caraco. Major role of marine vegetation on the oceanic carbon cycle. *Biogeosciences*, **2** (2005) 1–8.

[9] M.S. Fonseca and J.A. Cahalan, A preliminary evaluation of wave attenuation by four species of seagrass. *Estuar. Coast. Shelf Sci.* **35** (1992) 565–576.

[10] D. Gomila, P. Colet, G.-L. Oppo and M. San Miguel, Stable droplets and growth laws close to the modulational instability of a domain wall. *Phys. Rev. Lett.* **87** (2001) 194101.

[11] B.S. Halpern, K.A. Selkoe, F. Micheli and C.V. Kappel, Evaluating and ranking the vulnerability of global marine ecosystems to anthropogenic threats. *Conserv. Biol.* **21** (2007) 1301–1315.

[12] B.S. Halpern, S. Walbridge, K.A. Selkoe, C.V. Kappel, F. Micheli, C. D'Agrosa, J.F. Bruno, K.S. Casey, C. Ebert, H.E. Fox, R. Fujita, D. Heinemann, H.S. Lenihan, E.M.P. Madin, M.T. Perry, E.R. Selig, M. Spalding, R. Steneck and R. Watson, A global map of human impact on marine ecosystems. *Science* **319** (2008) 948–952.

[13] B. Hernádez-Bermejo and V. Fairén, Lotka–Volterra representation of general nonlinear systems. *Math. Biosci.* **140** (1997) 1–32.

[14] P.C. le Roux and M.A. McGeoch, Interaction intensity and importance along two stress gradients: adding shape to the stress-gradient hypothesis. *Oecologia* **162** (2010) 733–745.

[15] E. Llabrés, E. Mayol, N. Marbà and T. Sintes, A mathematical model for inter-specific interactions in seagrasses. *Oikos* **2022** (2022) e09296.

[16] E. Llabrés, A. Blanco-magad, M. Sales and T. Sintes, Modelling seagrass competition in the Mediterranean Sea in global warming scenarios. (2022).

[17] E. Mayol, J. Boada, M. Pérez, N. Sanmartí, M. Minguito-Frutos, R. Arthur, T. Alcoverro, D. Alonso and J. Romero, Understanding the depth limit of the seagrass Cymodocea nodosa as a critical transition: field and modeling evidence. *Mar. Environ. Res.* **182** (2022).

[18] K.J. McGlathery, M.A. Reidenbach, P. D'Odorico, S. Fagherazzi, M.L. Pace and J.H. Porter, Nonlinear dynamics and alternative stable states in shallow coastal systems. *Oceanography* **26** (2013) 220–231.

[19] P. Moreno-Spiegelberg, A. Arinyo-i Prats, D. Ruiz-Reynés, M.A. Matias and D. Gomila, Bifurcation structure of traveling pulses in type-I excitable media. *Phys. Rev. E* **106** (2022) 034206.

[20] R.J. Orth, T.J.B. Carruthers, W.C. Dennison, C.M. Duarte, J.W. Fourqurean, K.L. Heck, A. Randall Hughes, G.A. Kendrick, W.J. Kenworthy, S. Olyarnik, F.T. Short, M. Waycott and S.L. Williams, A global crisis for seagrass ecosystems. *Bioscience* **56** (2006) 987–996.

[21] A. Randall Hughes, S.L. Williams, C.M. Duarte, K.L. Heck and M. Waycott, Associations of concern: Declining seagrasses and threatened dependent species. *Front. Ecol. Environ.* **7** (2009) 242–246.

[22] M.L. Rosenzweig, Paradox of enrichment: destabilization of exploitation ecosystems in ecological time. *Science* **171** (1971) 385–387.

[23] D. Ruiz-Reynés, D. Gomila, T. Sintes, E. Hernández-García, N. Marbà and C.M. Duarte, Fairy circle landscapes under the sea. *Sci. Adv.* **3** (2017) 1–9.

[24] D. Ruiz-Reynés, F. Schönsberg, E. Hernández-García and D. Gomila, General model for vegetation patterns including rhizome growth. *Phys. Rev. Res.* **2** (2020) 1–8.

[25] V. Ryabinin, J. Barbière, P. Haugan, G. Kullenberg, N. Smith, C. McLean, A. Troisi, A. Fischer, S. Aricò, T. Aarup, P. Pissierssens, M. Visbeck, H.O. Enevoldsen and J. Rigaud, The UN decade of ocean science for sustainable development. *Front. Mar. Sci.* **6** (2019) 470.

[26] J.F. Sánchez-González, V. Sánchez-Rojas and C.D. Memos, Wave attenuation due to Posidonia oceanica meadows. *J. Hydraul. Res.* **49** (2011) 503–514.

[27] I. Savva, S. Bennett, G. Roca, G. Jordà and N. Marbà, Thermal tolerance of Mediterranean marine macrophytes: vulnerability to global warming. *Ecol. Evol.* **8** (2018) 12032–12043.

[28] T. Sintes, N. Marbà, C.M. Duarte and G.A. Kendrick, Nonlinear processes in seagrass colonisation explained by simple clonal growth rules. *Oikos* **108** (2005) 165–175.

[29] T. Sintes, N. Marbà and C.M. Duarte, Modeling nonlinear seagrass clonal growth: assessing the efficiency of space occupation across the seagrass flora. *Estuar. Coasts* **29** (2006) 72–80.

[30] M. Waycott, C.M. Duarte, T.J.B. Carruthers, R.J. Orth, W.C. Dennison, S. Olyarnik, A. Calladine, J.W. Fourqurean, K.L. Heck, A. Randall Hughes, G.A. Kendrick, W. Judson Kenworthy, F.T. Short and S.L. Williams, Accelerating loss of seagrasses across the globe threatens coastal ecosystems. *Proc. Natl. Acad. Sci. U.S.A.* **106** (2009) 12377–12381.